

*School of Natural Sciences and Mathematics
William B. Hanson Center for Space Sciences*

***Sequentially Bridged Graphene Sheets with High
Strength, Toughness, and Electrical Conductivity***

UT Dallas Author(s):

Jiuke Mu
Ali E. Aliev
Shaoli Fang
Ray H. Baughman

Rights:

CC BY-NC-ND 4.0 (Attribution-NonCommercial-NoDerivatives)
©2018 National Academy of Sciences. All Rights Reserved.

Citation:

Wan, S., Y. Li, J. Mu, A. E. Aliev, et al. 2018. "Sequentially bridged graphene sheets with high strength, toughness, and electrical conductivity." *Proceedings of the National Academy of Sciences of the United States of America* 115(21): 5359-5364, doi:10.1073/pnas.1719111115

This document is being made freely available by the Eugene McDermott Library of the University of Texas at Dallas with permission of the copyright owner. All rights are reserved under United States copyright law unless specified otherwise.

Sequentially bridged graphene sheets with high strength, toughness, and electrical conductivity

Sijie Wan^{a,b,1}, Yuchen Li^{a,b,1}, Jiuke Mu^{c,1}, Ali E. Aliev^c, Shaoli Fang^c, Nicholas A. Kotov^{b,d,e}, Lei Jiang^{a,b}, Qunfeng Cheng^{a,b,2}, and Ray H. Baughman^{c,2}

^aKey Laboratory of Bio-inspired Smart Interfacial Science and Technology of Ministry of Education, School of Chemistry, Beihang University, 100191 Beijing, People's Republic of China; ^bBeijing Advanced Innovation Center for Biomedical Engineering, Beihang University, 100191 Beijing, People's Republic of China; ^cAlan G. MacDiarmid NanoTech Institute, University of Texas at Dallas, Richardson, TX 75080; ^dDepartment of Chemical Engineering, University of Michigan, Ann Arbor, MI 48109; and ^eBiointerface Institute, University of Michigan, Ann Arbor, MI 48109

Edited by Frans Spaepen, Harvard University, Cambridge, MA, and accepted by Editorial Board Member Tobin J. Marks March 28, 2018 (received for review November 3, 2017)

We here show that infiltrated bridging agents can convert inexpensively fabricated graphene platelet sheets into high-performance materials, thereby avoiding the need for a polymer matrix. Two types of bridging agents were investigated for interconnecting graphene sheets, which attach to sheets by either π - π bonding or covalent bonding. When applied alone, the π - π bonding agent is most effective. However, successive application of the optimized ratio of π - π bonding and covalent bonding agents provides graphene sheets with the highest strength, toughness, fatigue resistance, electrical conductivity, electromagnetic interference shielding efficiency, and resistance to ultrasonic dissolution. Raman spectroscopy measurements of stress transfer to graphene platelets allow us to decipher the mechanisms of property improvement. In addition, the degree of orientation of graphene platelets increases with increasing effectiveness of the bonding agents, and the interlayer spacing increases. Compared with other materials that are strong in all directions within a sheet, the realized tensile strength (945 MPa) of the resin-free graphene platelet sheets was higher than for carbon nanotube or graphene platelet composites, and comparable to that of commercially available carbon fiber composites. The toughness of these composites, containing the combination of π - π bonding and covalent bonding, was much higher than for these other materials having high strengths for all in-plane directions, thereby opening the path to materials design of layered nanocomposites using multiple types of quantitatively engineered chemical bonds between nanoscale building blocks.

graphene nanocomposites | cross-linked graphene | graphene oxide | covalent bonding agents | π - π bonding agents

Carbon fiber reinforced polymer composites are becoming ubiquitous in automotive, aviation, electronic, energy, and biomedical technologies. However, carbon fiber composites have many shortcomings that make their broader utilization challenging from both technical and economic standpoints. First, the mechanical properties of carbon fiber composites are anisotropic even when carbon fiber sheets are plied. Secondly, delamination of carbon fiber from the polymer matrix, especially in the seams with other materials, causes fractures that lead to failures. Thirdly, the electrical conductivity of carbon fiber composites is lower than desired for some applications.

Carbon-based nanomaterials, such as individual carbon nanotubes (CNTs) (1) and single graphene sheet (2), show extremely high mechanical and electrical properties due to their sp^2 bonding and nearly defect-free structure (3, 4). In the past decade, starting from the early examples (5, 6), various graphene-based composites (7–9), including thin sheets comprising graphene platelets (10–13), have been fabricated. However, improvements in mechanical and electrical properties are needed before inexpensive graphene-based composites can be used for high-performance applications. Instead of making a polymer composite in which graphene platelets are uniformly layered in a host polymer, we are designing a structure in which covalent and π - π interplatelet bonding provides bridges between adjacent graphene layers, and no host polymer resin is needed.

Herein, we demonstrate the fabrication of high-performance graphene-based sheets and the general method for their molecular engineering using versatile bridging chemistries. Using graphene oxide (GO) or reduced graphene oxide (rGO) platelets as the precursor, either the GO or rGO was sequentially exposed to agents that could bridge through π - π interactions or covalent bonding. These two bridging elements were added independently, which is convenient for optimizing performance by controlling the relative ratio of π - π interactions and covalent bonding. As a result, mechanical load is effectively transferred between rGO platelets in sequentially bridged graphene (SBG) composites, providing high strength, toughness, and electrical conductivity. The macroscale effect of nanoscale bridging is observed by the simultaneous improvements of various mechanical properties, as well as electrical conductivity, stability in harsh environments, and microwave shielding capabilities. Raman measurements demonstrate on a molecular scale the stress transfer that results in properties improvements.

Results and Discussion

Fig. 14 illustrates the process used to make SBG sheets. First, GO (SI Appendix, Fig. S1) dispersed in water was vacuum filtered to

Significance

There is a continuing search for manufacturable sheets having high strength and toughness in all sheet directions for diverse applications, from airplanes to windmills. Cross-plied carbon fibers in a polymer resin requiring high-temperature cure presently provide the common solution. We demonstrate cross-linked graphene sheets that are manufacturable from graphene platelets, which are resin-free, processable at low temperature, contain less than 10 wt % additives, and provide high strength and record toughness in all in-plane directions. This advance results from successive use of π - π and covalent cross-linking agents. Simultaneous enhancement of strength, durability, and electrical conductivity are demonstrated. Spectroscopic measurements, including Raman studies of interplatelet stress transfer, elucidate the chemical nature and physical consequences of these dual cross-linking agents.

Author contributions: Q.C. designed research; S.W., Y.L., J.M., A.E.A., S.F., and R.H.B. performed research; J.M., S.F., N.A.K., L.J., Q.C., and R.H.B. analyzed data; and S.W., S.F., Q.C., and R.H.B. wrote the paper.

The authors declare no conflict of interest.

This article is a PNAS Direct Submission. F.S. is a guest editor invited by the Editorial Board.

This open access article is distributed under Creative Commons Attribution-NonCommercial-NoDerivatives License 4.0 (CC BY-NC-ND).

¹S.W., Y.L., and J.M. contributed equally to this work.

²To whom correspondence may be addressed. Email: cheng@buaa.edu.cn or Ray.Baughman@utdallas.edu.

This article contains supporting information online at www.pnas.org/lookup/suppl/doi:10.1073/pnas.1719111115/-DCSupplemental.

Published online May 7, 2018.

form a freestanding GO sheet. This sheet was immersed in a solution of 10,12-pentacosadiyn-1-ol [PCO, $\text{CH}_3(\text{CH}_2)_{11}\text{C}\equiv\text{C}-\text{C}\equiv\text{C}(\text{CH}_2)_8\text{CH}_2\text{OH}$] and then, after drying, exposed to UV light to provide a GO-PCO sheet in which the diacetylene groups of PCO have reacted by 1,4-addition polymerization (14, 15). Afterward, hydriodic acid (HI) was used to reduce the GO-PCO sheets into graphene-PCO (G-PCO) sheets. Finally, the G-PCO sheet was immersed successively into 1-pyrenebutyric acid *N*-hydroxysuccinimide ester (PSE) and 1-aminopyrene (AP) solutions, thereby providing an SBG sheet in which the PSE and AP have bonded through π - π interactions with neighboring graphene platelets and reacted to provide PSE-AP covalent bonds (16). The ratio of π - π interactions through PSE-AP derived bonding and covalent bonding resulting from PCO can be optimized by adjusting the immersion times in the respective solutions. To compare properties, sheets were also obtained by

eliminating treatment with PCO, thereby providing sheets that are π -bridged graphene (π BG).

The combination of these bridging agents, using optimized relative concentrations, provides the difficult-to-attain combination of strength and toughness for a structure having isotropic in-plane mechanical properties. Previous investigations led to our choice of the individual bridging agents. Over two decades ago, Katz (17) demonstrated the use of the strong π -bonding of PSE to pyrolytic graphite for protein immobilization, and deployed an extrusion reaction to enable direct coupling between the carbonyl group of PSE and a NH group of a protein, like for the present reaction with AP to form PSE-AP (Fig. 1A). AP is well known to strongly bond with graphitic surfaces (18). Using AP with another reactive π -bonding agent, thin sheets having a tensile strength of 539 MPa were obtained (19). Scanning tunneling microscopy has shown that the diacetylene monomer PCO polymerizes by 1,4-addition reaction on graphite sheets (20) and polymerized PCO has been used to increase the realized modest tensile strengths (220 MPa) for stretched CNT sheets (15). Polymerized PCO has also been used to cross-couple rGO nanosheets to provide a maximum tensile strength of 157 MPa (14).

Schematic illustrations are provided for 1,4-addition polymerization of PCO to yield covalent connectivity between platelet edges of rGO (Fig. 1B and *SI Appendix*, Fig. S2) and between the basal planes of neighboring graphene platelets (*SI Appendix*, Fig. S3). Spectroscopic evidence for these bridging processes and resulting property improvements will be described later. After PCO infiltration, the hydroxyl group on one end of the PCO monomers can covalently graft to GO nanosheets by reaction with carboxyl groups on the GO nanosheets. Then, PCO molecules grafted on nearby GO platelets are covalently coupled by 1,4-addition polymerization of diacetylene groups using UV irradiation (Fig. 1B and *SI Appendix*, Figs. S2 and S3). Subsequent HI reduction removes most of the unreacted oxygen-containing groups on the surface of GO nanosheets. After successive PSE and AP infiltration, the PSE and AP react to form PSE-AP (shown in Fig. 1B), which provides at opposite PSE-AP ends the aromatic functionalities needed for the π - π interactions that enable bridging between nearby rGO nanosheets.

Since X-ray diffraction measurements (*SI Appendix*, Table S1) indicate that the interplanar spacing within π - π bonded, covalently bonded, and sequentially bonded platelets are atomically thin (between 3.70 and 3.81 Å, and close to the 3.66 Å for dry rGO), it is clear that the PCO and PSE-AP bonding agents provide structural reinforcement by coating the surfaces of rGO platelets, rather than intercalating the platelets. These binding agents can thereby potentially connect platelet edges (both interplatelet and intraplatelet) and connect the exterior basal planes of stacked platelets. Since the ratio of the surface area available on exterior platelet basal planes to that on platelet edges is very large (on the order of 4,000, based on the measurement results in *SI Appendix*, Fig. S1 for exfoliated graphene oxide), we suspect that edge-based coupling (like exclusively illustrated in Fig. 1B for PCO-based covalent coupling) is unimportant. Moreover, the topochemical 1,4-addition polymerization of a diacetylene monomer critically depends on the assembly of PCO into an ordered array, and such assembly (illustrated in *SI Appendix*, Fig. S3) is likely facilitated by the roughly planar geometry of the exterior basal planes of GO platelets.

Five kinds of SBG sheets were prepared: SBG-I to SBG-V. The content of PSE-AP and PCO molecules (*SI Appendix*, Table S2) in these flexible silver-gray sheets (Fig. 1C) was derived from thermogravimetric analysis curves (*SI Appendix*, Fig. S4). Fig. 1D and E shows low- and high-resolution scanning electron microscope (SEM) images of SBG-V (containing 3.98 wt % PCO and 5.43 wt % PSE-AP), which are similar to the images for the other investigated SBG samples (*SI Appendix*, Fig. S5). The energy-dispersive X-ray spectroscopy mapping of nitrogen

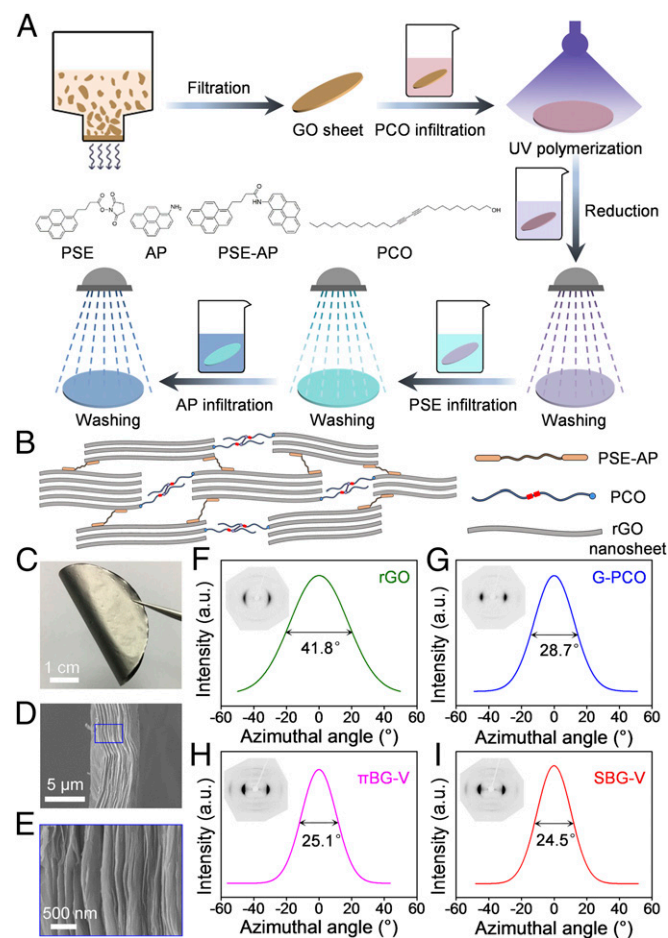


Fig. 1. Fabrication and structural characterization of SBG sheets. (A) GO platelets were assembled into a GO sheet by filtration, and then PCO was infiltrated into the GO sheet and polymerized using UV radiation. Next, the GO-PCO was reduced using HI. Afterward, PSE and AP were successively infiltrated into the sheet, which resulted in their reaction to form PSE-AP molecules, which are able to π -bond on rGO layers. (B) Schematic structural model showing possibly resulting edge connection between rGO layers in different platelets within an SBG sheet. *SI Appendix*, Fig. S3 illustrates 1,4-addition reaction of diacetylene layers on the top of a platelet, which can provide covalent bonding between neighboring platelet surfaces. (C) Photograph of an SBG sheet, showing its flexibility. (D) Low-resolution SEM image of the edge of a fractured SBG sheet. (E) High-resolution SEM image of the area outlined in D. WAXS patterns for an incident beam parallel to the sheet plane and corresponding azimuthal scan profiles for 002 peak for (F) rGO, (G) G-PCO, (H) π BG-V, and (I) SBG-V sheets.

Fig. 4. Dependence of Raman frequency down-shifts on applied strain. (A) rGO, (B) G-PCO, (C) μ BG-V, and (D) SBG-V sheets. Optical images of the sheets at zero strain are in the upper right-hand corners. The images in the below left-hand corners show the spatial distribution of Raman frequencies. All images are of a $400\text{-}\mu\text{m}^2$ square area. The scale bar indicates the relationship between the color in the images and the Raman frequency.

sacrificial bonds that break and reform dynamically during fatigue testing. Such behavior is similar to that of some tough biological materials (54), which are able to dissipate much more energy than materials having predominantly strong covalent bonding. This observation is conducive with biomimetic engineering of these layered compounds enhanced by optimized bridging. Stress-strain curves during cycling and fracture morphologies after fatigue fracture are shown in *SI Appendix, Fig. S20*.

Consistent with the improved organization of the graphene-based nanocomposites (55), the bridging also increases the electrical conductivity and the electromagnetic interference (EMI) shielding efficiency of rGO sheets. More specifically, the successively bridged sheet sample SBG-V provides the highest electrical conductivity ($512.3 \pm 24.5 \text{ S}\cdot\text{cm}^{-1}$, Fig. 3E and *SI Appendix, Table S4*), the highest gravimetric electrical conductivity ($247.5 \pm 11.8 \text{ S}\cdot\text{cm}^2\cdot\text{g}^{-1}$), and the highest EMI shielding efficiency (Fig. 3F). Note that the electrical conductivity of SBG-V sheets is lower than for recently reported high-temperature-annealed graphene sheets (11) and graphene sheet composites composed of almost-intact graphene nanosheets (30). For comparison, the electrical conductivity and gravimetric electrical conductivity of rGO, G-PCO, and π BG-V are $186.8 \pm 16.9 \text{ S}\cdot\text{cm}^{-1}$ and $92.9 \pm 8.4 \text{ S}\cdot\text{cm}^2\cdot\text{g}^{-1}$, $357.2 \pm 18.6 \text{ S}\cdot\text{cm}^{-1}$ and $176.0 \pm 9.2 \text{ S}\cdot\text{cm}^2\cdot\text{g}^{-1}$, and $440.5 \pm 21.3 \text{ S}\cdot\text{cm}^{-1}$ and $215.9 \pm 10.4 \text{ S}\cdot\text{cm}^2\cdot\text{g}^{-1}$, respectively. Reflecting the high electrical conductivity of SBG-V, the EMI shielding effectiveness of SBG-V sheets ($\sim 27 \text{ dB}$) in the frequency range between 0.3 and 12 GHz is higher than for similarly thick rGO ($\sim 11 \text{ dB}$), G-PCO ($\sim 16 \text{ dB}$), and π BG-V ($\sim 21 \text{ dB}$) sheets. While the EMI shielding efficiency of SBG-V sheets is inferior to other state-of-the-art EMI shielding materials (56), it is still higher than for previously reported graphene sheets (57–59) having similar thicknesses, and is in the range of commercial interest.

Raman measurements of the strain dependence (60) of the graphene G-band frequency provide interesting information on the differences in stress transfer for rGO, G-PCO, π BG-V, and SBG-V sheets (61–64) (Fig. 4). Both rGO and G-PCO provide long plateaus in which Raman frequency is independent of the macroscopically applied strain. This plateau is between $\sim 0.4\%$ and $\sim 2.5\%$ strain for rGO sheets and between $\sim 0.6\%$ and $\sim 5\%$ strain for G-PCO sheets, where the upper strain limit corresponds to sheet fracture for rGO and is slightly below the strain of complete fracture for G-PCO ($\sim 5.8\%$). These results show that while PCO substantially increases the strain to failure, it does not enable efficient stress transfer to the graphene sheets in the plateau region. In contrast, the π BG-V and SBG-V sheets do not have a plateau region in Raman frequency shift. This fact and the larger strain dependence of Raman shift for π BG-V and SBG-V sheets than for rGO or G-PCO sheets indicate more efficient stress transfer to the graphene sheets. Note that the failure stress and the Raman frequency shift up to failure strain are 209.7 MPa and $\sim 1.2 \text{ cm}^{-1}$ for rGO, 348.5 MPa and $\sim 5.6 \text{ cm}^{-1}$ for G-PCO, 688.5 MPa and $\sim 13.2 \text{ cm}^{-1}$ for π BG-V, and 944.5 MPa and $\sim 15.7 \text{ cm}^{-1}$ for SBG-V. Hence, both the observed Raman shifts and the measured tensile strength indicate improved stress transfer for π BG-V and SBG-V sheets compared with that for rGO and G-PCO sheets.

The Raman frequency shifts are reversible for all of the presently investigated graphene sheet compositions as long as

the applied strain does not exceed $\sim 0.4\%$ (*SI Appendix, Fig. S21*), which might correspond to elastic deformability due to straightening of rGO platelets. While there is no significant higher strain range where strain release reverses without hysteresis the strain-induced Raman frequency down-shift for rGO, this strain range exists for strains down to $\sim 5.4\%$ for G-PCO stretched to 5.75%, for strains down to $\sim 1.5\%$ for π BG-V stretched to 2.0%, and for strains down to $\sim 2.9\%$ for SBG-V stretched to 3.4%. This elastic behavior with respect to the stretch applied to the graphene sheets (as measured by Raman frequency shifts) might result from elastic strain release due to covalent bonding, π - π bonding, and some combination of π - π and covalent bonding.

The sequential application of two bridging agents has enabled the scalable fabrication of resin-free composites having a combination of multiple properties including both mechanical and charge-transport characteristics. The realized tensile strength (945 MPa) exceeds that of previously reported CNT or graphene platelet composites that are strong in all sheet plane directions, and is comparable to that of commercially available carbon fiber sheet composites that are plied to increase strength in all in-plane directions. The toughness of our composites containing the combination of π - π bonding and covalent bonding bridging agents is more effective than the application of either agent. The strain dependence of Raman frequency indicate the effectiveness of π -bonded and covalently bonded agents in distributing local stress and can help address fundamental questions about structural relationship between nano-sheet interfaces and the macroscale mechanics of biomimetic composites. SBG composites might provide the next generation of lightweight functional composites that are needed for addressing the problems facing several key industries.

Materials and Methods

The PCO was received from Tokyo Chemical Industry Co., Ltd., and PSE, AP, and HI (57 wt %) were purchased from Sigma-Aldrich. THF ($\geq 99.0\%$), NMP ($\geq 99.0\%$), DMF ($\geq 99.5\%$), H_2SO_4 , NaOH, and ethanol ($\geq 99.7\%$) were obtained from Sino-pharm Chemical Reagents Co., Ltd. These reagents were used as received without further purification. Deionized water (resistivity $> 18 \text{ M}\Omega\cdot\text{cm}$) was collected from a Milli-Q Biocel system. GO was prepared by modified Hummer's method (12) and dried for the following experiments. More details on the materials and methods can be found in *SI Appendix*.

ACKNOWLEDGMENTS. We thank Professor Juan José Vilatela at Madrid Institute for Advanced Studies of Materials for WAXS measurements, and thank Professor Jiaxing Huang at Northwestern University for helpful discussion. This work was supported by the Excellent Young Scientist Foundation of the National Natural Science Foundation of China (NSFC) (Grant 51522301), the NSFC (Grants 21273017 and 51103004), the Program for New Century Excellent Talents in University (Grant NCET-12-0034), the Fok Ying-Tong Education Foundation (Grant 141045), the 111 Project (Grant B14009), the Aeronautical Science Foundation of China (Grants 20145251035 and 20152F21009), State Key Laboratory of Organic-Inorganic Composites, Beijing University of Chemical Technology (Grant oic-201701007), the State Key Laboratory for Modification of Chemical Fibers and Polymer Materials, Donghua University (Grant LK1710), the Fundamental Research Funds for the Central Universities (Grants YWF-16-BJ-J-09 and YWF-17-BJ-J-33), and the Academic Excellence Foundation of Beihang University for PhD Students. Support in the United States was from Air Force Office of Scientific Research Grants FA9550-15-1-0089 and FA9550-12-1-0035 and NSF Award 1636306.

- Iijima S (1991) Helical microtubules of graphitic carbon. *Nature* 354:56–58.
- Novoselov KS, et al. (2004) Electric field effect in atomically thin carbon films. *Science* 306:666–669.
- Du X, Skachko I, Barker A, Andrei EY (2008) Approaching ballistic transport in suspended graphene. *Nat Nanotechnol* 3:491–495.
- Lee C, Wei X, Kysar JW, Hone J (2008) Measurement of the elastic properties and intrinsic strength of monolayer graphene. *Science* 321:385–388.
- Kotov NA, Dekány I, Fendler JH (1996) Ultrathin graphite oxide–polyelectrolyte composites prepared by self-assembly: Transition between conductive and non-conductive states. *Adv Mater* 8:637–641.

- Mamedov AA, et al. (2002) Molecular design of strong single-wall carbon nanotube/polyelectrolyte multilayer composites. *Nat Mater* 1:190–194.
- Wan SJ, Cheng QF (2017) Fatigue-resistant bioinspired graphene-based nanocomposites. *Adv Funct Mater* 27:1703459.
- Wan S, Peng J, Jiang L, Cheng Q (2016) Bioinspired graphene-based nanocomposites and their application in flexible energy devices. *Adv Mater* 28:7862–7898.
- Zhang Y, et al. (2016) Graphene-based artificial nacre nanocomposites. *Chem Soc Rev* 45:2378–2395.
- Xiao Y, et al. (2017) Sheet collapsing approach for rubber-like graphene papers. *ACS Nano* 11:8092–8102.

11. Peng L, et al. (2017) Ultrahigh thermal conductive yet superflexible graphene films. *Adv Mater* 29:1700589.
12. Zhang M, et al. (2015) Multifunctional pristine chemically modified graphene films as strong as stainless steel. *Adv Mater* 27:6708–6713.
13. Liu Z, et al. (2014) Wet-spun continuous graphene films. *Chem Mater* 26:6786–6795.
14. Cheng Q, Wu M, Li M, Jiang L, Tang Z (2013) Ultratough artificial nacre based on conjugated cross-linked graphene oxide. *Angew Chem Int Ed Engl* 52:3750–3755.
15. Chen IWP, Liang R, Zhao H, Wang B, Zhang C (2011) Highly conductive carbon nanotube buckypapers with improved doping stability via conjugational cross-linking. *Nanotechnology* 22:485708.
16. Chen IWP (2013) Noncovalently functionalized highly conducting carbon nanotube films with enhanced doping stability via an amide linkage. *Chem Commun (Camb)* 49:2753–2755.
17. Katz E (1994) Application of bifunctional reagents for immobilization of proteins on a carbon electrode surface: Oriented immobilization of photosynthetic reaction centers. *J Electroanal Chem* 365:157–164.
18. Wang S, Wang X, Jiang SP (2008) PtRu nanoparticles supported on 1-aminopyrene-functionalized multiwalled carbon nanotubes and their electrocatalytic activity for methanol oxidation. *Langmuir* 24:10505–10512.
19. Ni H, et al. (2017) Robust bioinspired graphene film via π - π cross-linking. *ACS Appl Mater Interfaces* 9:24987–24992.
20. Takajo D, Inaba A, Sudoh K (2014) Two-dimensional solid-state topochemical reactions of 10,12-pentacosadiyn-1-ol adsorbed on graphite. *Langmuir* 30:2738–2744.
21. Wegst UGK, Bai H, Saiz E, Tomsia AP, Ritchie RO (2015) Bioinspired structural materials. *Nat Mater* 14:23–36.
22. Coleman JN (2013) Liquid exfoliation of defect-free graphene. *Acc Chem Res* 46:14–22.
23. Hernandez Y, et al. (2008) High-yield production of graphene by liquid-phase exfoliation of graphite. *Nat Nanotechnol* 3:563–568.
24. Cui W, et al. (2014) A strong integrated strength and toughness artificial nacre based on dopamine cross-linked graphene oxide. *ACS Nano* 8:9511–9517.
25. Gong S, et al. (2015) Integrated ternary bioinspired nanocomposites via synergistic toughening of reduced graphene oxide and double-walled carbon nanotubes. *ACS Nano* 9:11568–11573.
26. Wan S, et al. (2015) Synergistic toughening of graphene oxide-molybdenum disulfide-thermoplastic polyurethane ternary artificial nacre. *ACS Nano* 9:708–714.
27. Wan S, et al. (2015) Use of synergistic interactions to fabricate strong, tough, and conductive artificial nacre based on graphene oxide and chitosan. *ACS Nano* 9:9830–9836.
28. Wan S, et al. (2017) Fatigue resistant bioinspired composite from synergistic two-dimensional nanocomponents. *ACS Nano* 11:7074–7083.
29. Li YQ, Yu T, Yang TY, Zheng LX, Liao K (2012) Bio-inspired nacre-like composite films based on graphene with superior mechanical, electrical, and biocompatible properties. *Adv Mater* 24:3426–3431.
30. Wen Y, Wu M, Zhang M, Li C, Shi G (2017) Topological design of ultrastrong and highly conductive graphene films. *Adv Mater* 29:1702831.
31. Xiong R, et al. (2016) Ultrarobust transparent cellulose nanocrystal-graphene membranes with high electrical conductivity. *Adv Mater* 28:1501–1509.
32. Zhang M, Huang L, Chen J, Li C, Shi G (2014) Ultratough, ultrastrong, and highly conductive graphene films with arbitrary sizes. *Adv Mater* 26:7588–7592.
33. Wan SJ, Xu FY, Jiang L, Cheng QF (2017) Superior fatigue resistant bioinspired graphene-based nanocomposite via synergistic interfacial interactions. *Adv Funct Mater* 27:1605636.
34. Hu K, et al. (2013) Written-in conductive patterns on robust graphene oxide biopaper by electrochemical microstamping. *Angew Chem Int Ed Engl* 52:13784–13788.
35. Ming P, et al. (2015) Nacre-inspired integrated nanocomposites with fire retardant properties by graphene oxide and montmorillonite. *J Mater Chem A* 3:21194–21200.
36. Wan S, et al. (2016) Nacre-inspired integrated strong and tough reduced graphene oxide-poly(acrylic acid) nanocomposites. *Nanoscale* 8:5649–5656.
37. Zhang Q, Wan SJ, Jiang L, Cheng QF (2017) Bioinspired robust nanocomposites of cooper ions and hydroxypropyl cellulose synergistic toughening graphene oxide. *Sci China Technol Sci* 60:758–764.
38. Cheng QF, et al. (2009) High mechanical performance composite conductor: Multi-walled carbon nanotube sheet/bismaleimide nanocomposites. *Adv Funct Mater* 19:3219–3225.
39. Cheng Q, Li M, Jiang L, Tang Z (2012) Bioinspired layered composites based on flat-tented double-walled carbon nanotubes. *Adv Mater* 24:1838–1843.
40. Coleman JN, et al. (2003) Improving the mechanical properties of single-walled carbon nanotube sheets by intercalation of polymeric adhesives. *Appl Phys Lett* 82:1682–1684.
41. Olek M, et al. (2004) Layer-by-layer assembled composites from multiwall carbon nanotubes with different morphologies. *Nano Lett* 4:1889–1895.
42. Li J, et al. (2011) High performance, freestanding and superthin carbon nanotube/epoxy nanocomposite films. *Nanoscale* 3:3731–3736.
43. Shin MK, et al. (2012) Synergistic toughening of composite fibres by self-alignment of reduced graphene oxide and carbon nanotubes. *Nat Commun* 3:650–657.
44. Jiang S, et al. (2017) Ultrastrong steel via minimal lattice misfit and high-density nanoprecipitation. *Nature* 544:460–464.
45. Wu G, Chan K-C, Zhu L, Sun L, Lu J (2017) Dual-phase nanostructuring as a route to high-strength magnesium alloys. *Nature* 545:80–83.
46. Ren ZJ, Xue GX (2007) *Practical Handbook for Metal Materials* (Jiangsu Science and Technology Press, Nanjing, China). Chinese.
47. Kim S-H, Kim H, Kim NJ (2015) Brittle intermetallic compound makes ultrastrong low-density steel with large ductility. *Nature* 518:77–79.
48. He BB, et al. (2017) High dislocation density-induced large ductility in deformed and partitioned steels. *Science* 357:1029–1032.
49. Melveger AJ, Baughman RH (1973) Raman spectral changes during the solid-state polymerization of diacetylenes. *J Polym Sci B Polym Phys* 11:603–619.
50. Barentsen HM, van Dijk M, Kimkes P, Zuilhof H, Sudhölter EJR (1999) Dye-substituted acetylenes and diacetylenes: Convenient polymerization as studied by differential scanning calorimetry, FT-IR, and UV-vis spectroscopy. *Macromolecules* 32:1753–1762.
51. Pei SF, Zhao JP, Du JH, Ren WC, Cheng HM (2010) Direct reduction of graphene oxide films into highly conductive and flexible graphene films by hydrohalic acids. *Carbon* 48:4466–4474.
52. Stankovich S, et al. (2007) Synthesis of graphene-based nanosheets via chemical reduction of exfoliated graphite oxide. *Carbon* 45:1558–1565.
53. Moon IK, Lee J, Ruoff RS, Lee H (2010) Reduced graphene oxide by chemical graphitization. *Nat Commun* 1:73.
54. Barthelat F, Yin Z, Buehler MJ (2016) Structure and mechanics of interfaces in biological materials. *Nat Rev Mater* 1:16007.
55. Zhu J, Zhang H, Kotov NA (2013) Thermodynamic and structural insights into nanocomposites engineering by comparing two materials assembly techniques for graphene. *ACS Nano* 7:4818–4829.
56. Shahzad F, et al. (2016) Electromagnetic interference shielding with 2D transition metal carbides (MXenes). *Science* 353:1137–1140.
57. Shen B, Zhai WT, Zheng WG (2014) Ultrathin flexible graphene film: An excellent thermal conducting material with efficient EMI shielding. *Adv Funct Mater* 24:4542–4548.
58. Kumar P, et al. (2015) Large-area reduced graphene oxide thin film with excellent thermal conductivity and electromagnetic interference shielding effectiveness. *Carbon* 94:494–500.
59. Ye SB, Chen B, Hu DD, Liu CZ, Feng JC (2016) Graphene-based films with integrated strength and toughness via a novel two-step method combining gel casting and surface crosslinking. *ChemNanoMat* 2:816–821.
60. Mohiuddin TMG, et al. (2009) Uniaxial strain in graphene by Raman spectroscopy: G peak splitting, Grüneisen parameters, and sample orientation. *Phys Rev B* 79:205433.
61. Gao Y, et al. (2011) The effect of interlayer adhesion on the mechanical behaviors of macroscopic graphene oxide papers. *ACS Nano* 5:2134–2141.
62. Liu LQ, Barber AH, Nuriel S, Wagner HD (2005) Mechanical properties of functionalized single-walled carbon-nanotube/poly(vinyl alcohol) nanocomposites. *Adv Funct Mater* 15:975–980.
63. Lachman N, et al. (2009) Raman response of carbon nanotube/PVA fibers under strain. *J Phys Chem C* 113:4751–4754.
64. Mu M, Osswald S, Gogotsi Y, Winey KI (2009) An in situ Raman spectroscopy study of stress transfer between carbon nanotubes and polymer. *Nanotechnology* 20:335703.